

OPEN ACCESS

Spray Drying-Assisted Synthesis of $\text{Li}_3\text{VO}_4/\text{C}/\text{CNTs}$ Composites for High-Performance Lithium Ion Battery Anodes

To cite this article: Yang Yang *et al* 2017 *J. Electrochem. Soc.* **164** A6001

View the [article online](#) for updates and enhancements.



FOCUS ISSUE OF SELECTED PAPERS FROM IMLB 2016 WITH INVITED PAPERS CELEBRATING 25 YEARS OF LITHIUM ION BATTERIES

Spray Drying-Assisted Synthesis of $\text{Li}_3\text{VO}_4/\text{C}/\text{CNTs}$ Composites for High-Performance Lithium Ion Battery Anodes

Yang Yang, Jiaqi Li, Dingqiong Chen, and Jinbao Zhao^{*,z}

State Key Laboratory of Physical Chemistry of Solid Surfaces, College of Chemistry and Chemical Engineering, Collaborative Innovation Center of Chemistry for Energy Materials, Xiamen University, Xiamen 361005, People's Republic of China

Li_3VO_4 is a promising insertion anode material for lithium ion batteries (LIBs), but has the drawback of low electronic conductivity. Here, we have developed a facile spray drying route to synthesize $\text{Li}_3\text{VO}_4/\text{C}/\text{CNTs}$ (carbon nanotubes) composites with hollow spherical morphology. In this composite, Li_3VO_4 nanocrystals are interconnected by CNTs to form an integrated electronic conducting particle. Owing to the high specific surface and hierarchical porous structure, $\text{Li}_3\text{VO}_4/\text{C}/\text{CNTs}$ composites also possess higher apparent Li^+ ions diffusion coefficient. The resulting $\text{Li}_3\text{VO}_4/\text{C}/\text{CNTs}$ composites exhibit much better rate capability than the pristine Li_3VO_4 . A high reversible capacity of 272 mAh g^{-1} can be maintained up to 500 cycles at 10 C (86.1% retention of the 2nd charge capacity). Moreover, the synthetic method is facile and scalable, thus as-prepared LVO/C/CNTs composites can be a promising anode material for high-safety LIBs.

© The Author(s) 2016. Published by ECS. This is an open access article distributed under the terms of the Creative Commons Attribution 4.0 License (CC BY, <http://creativecommons.org/licenses/by/4.0/>), which permits unrestricted reuse of the work in any medium, provided the original work is properly cited. [DOI: 10.1149/2.0031701jes] All rights reserved.

Manuscript submitted June 7, 2016; revised manuscript received August 8, 2016. Published August 31, 2016. This was Paper 880 presented at the Chicago, Illinois, Meeting of the IMLB, June 19–24, 2016. *This paper is part of the Focus Issue of Selected Papers from IMLB 2016 with Invited Papers Celebrating 25 Years of Lithium Ion Batteries.*

Since lithium ion batteries (LIBs) were commercialized by Sony Corporation in June 1991,¹ LIBs have been the dominant power supply in portable electronic devices market due to their high energy density.² But owing to the rapid enlarging markets of large-sized applications like electric vehicles and stationary energy storage, there is an increasing demand for LIBs with safer operation and longer cycle-life.³ Nowadays, graphite-based materials are still the most common anode materials in commercial LIBs. However, the practical application of graphite anode in large-sized LIBs is hindered by its security issues.⁴ Because lithium dendrite could grow on the surface of anode during the overcharge or high rate charge process owing to a low Li-intercalation potential ($<0.1 \text{ V}$ vs Li^+/Li) of the graphite. Thus many researches have been focused on developing high-safety anode materials.^{5–7}

Recently, Li_3VO_4 has been studied as a new insertion anode.⁸ The crystal structure of Li_3VO_4 is illustrated in Figure 1. Li_3VO_4 crystallizes in the orthorhombic phase, and consists of corner-shared VO_4 and LiO_4 tetrahedrons.⁹ There are many empty cationic sites in the hollow lantern-like structure, which are expected to be intercalated with lithium ions.^{10,11} Combined with V^{5+} to V^{3+} reduction, Li_3VO_4 can deliver a theoretical capacity of 394 mAh g^{-1} , corresponding to $x = 2$ in $\text{Li}_{3+x}\text{VO}_4$. More importantly, the working voltage of Li_3VO_4 is mainly between $0.5 \sim 0.8 \text{ V}$ (vs Li^+/Li), meaning the growth of lithium dendrite is avoided intrinsically. Owing to the high-safety, Li_3VO_4 can be one of the most promising anode candidates for large-sized LIBs. However, its poor rate capability due to the low electronic conductivity ($\sim 5.8 \times 10^{-6} \text{ S cm}^{-1}$) impedes its wide use. To overcome this problem, extensive studies have been proposed to fabricate $\text{Li}_3\text{VO}_4/\text{C}$ composites, such as carbon-encapsulated Li_3VO_4 particles,^{10,12} $\text{Li}_3\text{VO}_4/\text{N}$ doped C,¹³ $\text{Li}_3\text{VO}_4/\text{graphene}$,^{11,14,15} $\text{Li}_3\text{VO}_4/\text{expanded graphite}$,¹⁶ and $\text{Li}_3\text{VO}_4/\text{CNTs}$.¹⁷ All these studies indicated that the introduction of carbon-based materials can effectively increase the electronic conductivity of the composite material, leading to high electrochemical performance. However, it is still needed to develop a more facile and scalable route to synthesize $\text{Li}_3\text{VO}_4/\text{C}$ composites with high performance for practical LIBs application.

In this work, we report a facile process for the synthesis of hollow $\text{Li}_3\text{VO}_4/\text{C}/\text{CNTs}$ (LVO/C/CNTs) composites by a simple one-pot spray drying process and subsequent heat-treatment. Hollow and porous structure can shorten diffusion paths of Li^+ ions and enhance

the penetration of electrolyte, leading to faster diffusion of Li^+ ions.¹⁸ The carbon layer coated on the surface of Li_3VO_4 particles can enhance the electronic conductivity. Moreover, CNTs were also introduced, which are connected to form conducting network inside this composites. The simultaneous enhancement of both electrons and Li^+ ions transfer can improve electrode kinetics, leading to a greatly improved rate capability and cycle stability.

Experimental

The LVO/C/CNTs composites were fabricated by using a spray drying process and subsequent heat-treatment in inertial atmosphere. In a typical experiment, 2.86 mmol (0.52 g) V_2O_5 , 8.58 mmol (0.633 g) Li_2CO_3 , 1.5 g CNTs aqueous dispersion (wt% = 10%, Timesnano) and 0.4 g glucose were added into 100 ml distilled water. After stirring overnight, the resulting solution was spray dried by using a Buchi mini spray drier B-290. The spray drying conditions were as follows: the inlet temperature: 205°C , the aspirator rate: 100%, the rotameter setting: 40 mm , and the pump rate: 5% (1.5 mL min^{-1}). Nitrogen was used as the carrier gas. The precursors obtained by the spray drying process were annealed at 600°C for 10 h under Ar atmosphere at the heating rate of 5°C min^{-1} . The pristine Li_3VO_4 (LVO) was also prepared as below: 2.86 mmol (0.52 g) V_2O_5 and 8.58 mmol (0.633 g) Li_2CO_3 were added into 100 ml distilled water. After stirring overnight, the resulting clear solution was dried in an oil-bath at 90°C and then annealed at 600°C in air for 10 h at the heating rate of 5°C min^{-1} .

X-ray diffraction (XRD) data were obtained on a Rigaku miniflex 600 instrument by using $\text{Cu K}\alpha$ radiation ($\lambda = 0.154 \text{ nm}$). Thermo gravimetric analysis (TGA) was taken on SDT Q600 (TA Instruments) under air flow ($20 \sim 800^\circ\text{C}$, $10^\circ\text{C min}^{-1}$). The nitrogen adsorption and desorption isotherms were attained by using the Brunauer-Emmett-Teller (BET, Micromeritics surface area and porosity analyzer, ASAP 2020) method. The morphological features of the samples were investigated by field emission scanning electronic microscopy (SEM, HITACHI S-4800) and high-resolution transmission electron microscopy (HRTEM, FEI TECNAI G2 F30).

Electrochemical performance of the samples was tested in a form of coin cell. Coin type cells (CR2016) were used for half cell fabrication. Metal lithium foil was used as both counter and reference electrodes. Celgard 2400 membrane was used as the separator. The electrolyte was 1 M LiPF_6 dissolved in the mixture of ethylene carbonate (EC) / diethyl carbonate (DEC) (v/v = 1:1). The working electrode

*Electrochemical Society Member.

^zE-mail: jbzha@xmu.edu.cn

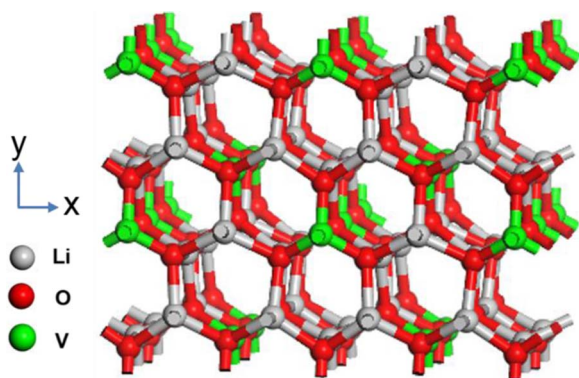


Figure 1. Crystal structure of Li_3VO_4 .

film was obtained by casting the slurry composed of active material, acetylene black, and polyvinylidene difluoride (PVDF) binder (weight ratio of 7:2:1) dispersed in *N*-methyl pyrrolidone (NMP) solvent onto a Cu foil followed by drying in a vacuum oven at 80°C overnight. Finally, the electrode was punched into discs and roll-pressed. The mass loading of the active material was approximately 0.5 ~ 1.0 mg cm^{-2} . Coin type cells (CR2032) were used for full cell fabrication. The LVO/C/CNTs electrode was used as the anode. The cathode was fabricated by coating the slurry composed of $\text{LiNi}_{0.5}\text{Co}_{0.2}\text{Mn}_{0.3}\text{O}_2$, acetylene black, and PVDF binder (weight ratio of 8:1:1) dispersed in NMP solvent onto an Al foil followed by drying in a vacuum oven at 80°C overnight. The cells with capacity limited by $\text{Li}_3\text{VO}_4/\text{C}/\text{CNTs}$ were galvanostatically cycled between 1.5 and 4.3 V. The charge-discharge cycling tests were conducted on a battery cycler (Neware BTS battery charger, Shenzhen, China). Electrochemical impedance spectra (EIS) tests were conducted at the on the electrochemical workstation of Solartron SI 1287, the frequency was set in the range from 0.01 Hz to 100 kHz. The cyclic voltammetry (CV) measurements were carried out by using the electrochemical workstation of Metrohm Autolab PGSTAT 302N.

Results and Discussion

The solution with Li_3VO_4 stoichiometry ($\text{Li}/\text{V} = 3$), glucose, and CNTs were prepared for spray drying. The aerosol droplets are generated from the nozzle, and then enter the droplet-to-particle conversion chamber (spray cylinder) via the carrier gas flow. After entering the cyclone, the carrier gas is separated, and the dried particles remain in the collecting vessel. From a droplet to a dried particle, just approximately 1 second is needed. Theoretically, if the drying speed of a sprayed droplet is sufficiently slow, the solute within the droplet will have sufficient time to redistribute, that will produce dense dried

particles.¹⁹ However, in our experiment, the high spray drying temperature and short residence induced by the high inlet temperature (205°C, which is much higher than the boil point of water) and high carrier gas flow (aspirator rate of 100%) result in fast evaporation rate. Therefore, the drying speed of the aerosol droplet is so quick that the solute does not have adequate time to redistribute and diffuse from the surface to the center of the droplet, and has to accumulate near the drying front of the droplet (the external surface of the droplet, that directly contacted with the hot carrier gas) instead.²⁰ At the end of the droplet-to-particle conversion process the evaporating front becomes a shell and form hollow structure.

The XRD patterns in Figure 2a indicate that both LVO/C/CNTs and LVO are coherent with the electrochemically active orthorhombic Li_3VO_4 β polymorph,²¹ which is in good agreement with the JCPDS, No. 38-1247. The TG curve of LVO/C/CNTs under air flow is shown in Figure 2b. The weight change of LVO/C under 200°C should be ascribed to the elimination of absorbed water,¹³ and the weight loss between 200°C and 700°C could attribute to the combustion of carbon (amorphous carbon and CNTs). Thus the carbon content of LVO/C/CNTs composites is calculated to be 20.9%.

The specific BET surface area of LVO/C/CNTs is 75.15 $\text{m}^2 \text{g}^{-1}$, which is much higher than that of LVO (0.267 $\text{m}^2 \text{g}^{-1}$). The N_2 adsorption-desorption isotherms of LVO/C/CNTs are shown in Figure 3a. The nitrogen adsorption below $P/P^0 = 0.1$ is a feature of micropores filling. The hysteresis loop and the continuous rise of the adsorption curve in the P/P^0 range from 0.1 to 1 derive from the existence of mesopores (0.1–0.6) and macropores (0.6–1) in the LVO/C/CNTs.^{22–24} Figure 3b displays the Barrett-Joyner-Halenda (BJH) pore-size distributions of LVO/C/CNTs. A broad peak from 1.9 to 52.7 nm indicates that the LVO/C/CNTs mainly possesses mesopores and a small number of micropores and macropores. The pore size distribution is not uniform, but it exhibits a hierarchical feature. This kind of hierarchically porous LVO/C/CNTs material is expected to facilitate the penetration of electrolyte and lithium ions transfer, leading to better electrochemical performance.^{7,22,25,26}

LVO/C/CNTs composites have a spherical shape (Figure 4a) with 0.5 ~ 8 μm in size. CNTs can be obviously observed on the surface of LVO/C/CNTs particles (Figure 4b). The TEM image (Figure 4d) clearly reveals the hollow structure of LVO/C/CNTs composites, which can be further confirmed in the High-angle annular dark field image (Figure 4c). TEM images shown in Figures 4d and 4e reveal that Li_3VO_4 nanocrystals are interconnected by CNTs and uniformly dispersed in the hollow spherical structure. Inset in Figure 4d is the SAED pattern of the LVO/C/CNTs particle. Irregular diffraction spots imply the polycrystalline structure of the LVO, while the regular diffraction rings should correspond to CNTs in the composite. The high resolution TEM image (Figure 4f) displays clear lattice fringes inside. The interplanar distance is measured to be 0.21 nm, which corresponds to the (112) faces of orthorhombic Li_3VO_4 . Meanwhile,

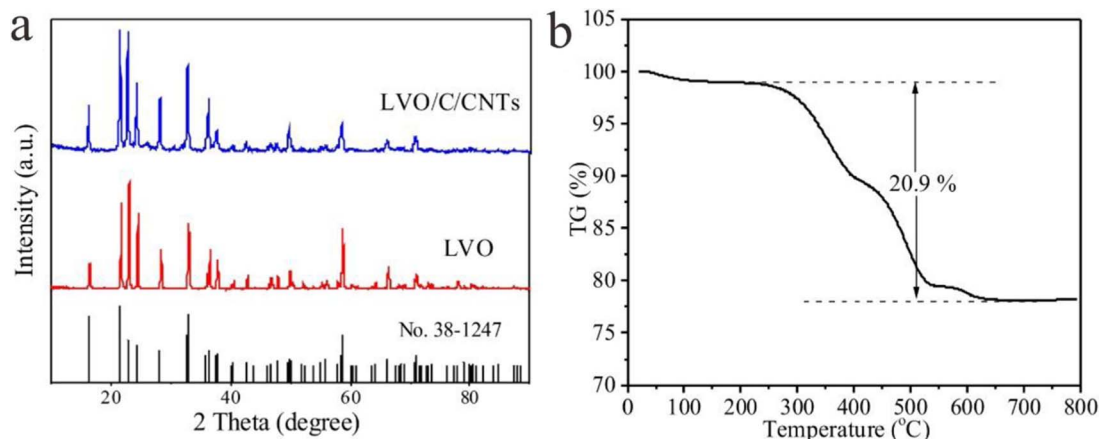


Figure 2. (a) XRD patterns of LVO/C/CNTs and LVO. (b) Thermo gravimetric (TG) curve of LVO/C/CNTs under air atmosphere.

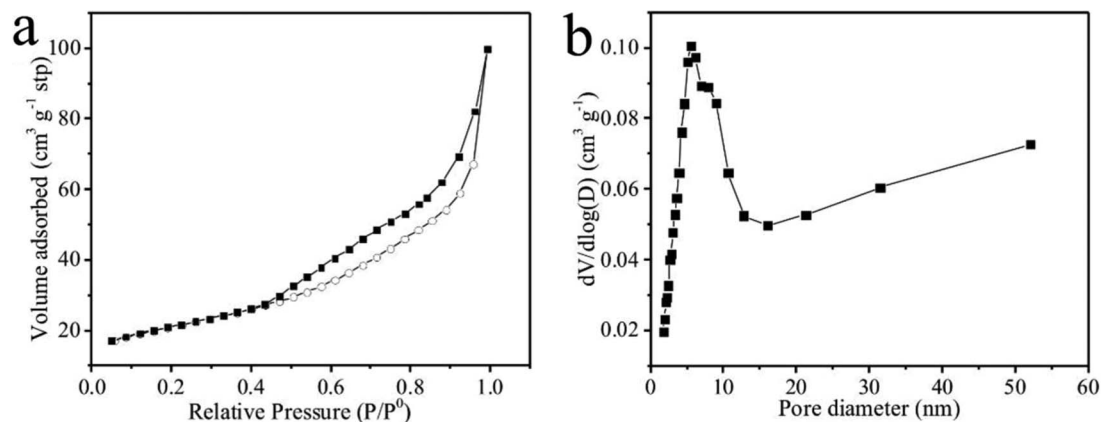


Figure 3. (a) N₂ adsorption-desorption isotherms, and (b) pore-size distributions of LVO/C/CNTs.

amorphous carbon layer mixed with CNTs (wrinkles in Figure 4f) are observed on the surface of the Li₃VO₄ nanocrystal. The amorphous carbon coating layers derives from the carbonization of glucose accompanied by the formation of Li₃VO₄ in the heat-treatment process. The CNTs are connected to construct a conducting network between these Li₃VO₄ nanocrystals and improve the electronic conductivity of the composites.

Half cells with metal lithium foil counter electrode were used to evaluate the electrochemical performance of LVO/C/CNTs and LVO as anodes for LIBs. Figure 5a shows CV curves of LVO/C/CNTs in the first 3 cycles at the sweep rate of 0.2 mV s⁻¹ between 0.2 to 2.0 V. For the first cathodic process, two obvious reduction peaks at the potentials of 0.69 and 0.51 V are observed, which associate with the reduction of V⁵⁺ to V³⁺. These two peaks shift to 0.84 and 0.50 V in the subsequent cycles, which may be ascribed to the activation of the LVO/C/CNT electrode.^{27,28} The curves for the first three anodic processes are similar, exhibiting a broad oxidation peak at around 1.3 V, which associate with the oxidation of V³⁺ to V⁵⁺.¹⁴ The lithiation and delithiation processes can be described as Equation 1.

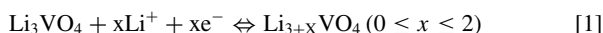


Figure 5b shows charge-discharge voltage profiles of LVO/C/CNTs in the first 3 cycles at 0.5 C between 0.2 to 2.0 V. LVO/C/CNTs is intercalated by Li⁺ ions mainly at the voltage between 0.5 and 1.5 V, lower than Li₄Ti₅O₁₂, and higher than graphite. The initial discharge and charge capacities are 658 and 397 mAh g⁻¹, corresponding to an initial coulombic efficiency of 60.4%. The irreversible capacity loss may result from the formation of a solid electrolyte interface (SEI) layer.¹⁴

Rate capability is very important especially for applications in large-size LIBs.²⁹ The rate capability of the LVO/C/CNTs and LVO under different current densities of 0.5 ~ 50 C are shown in Figure 6a. Obviously, the LVO/C/CNTs exhibits much improved rate performance than LVO especially at a high rate. The LVO/C/CNTs shows the average charge capacity of 391 mAh g⁻¹ at 0.5 C. At higher current densities of 1 C, 5 C, 10 C, and 20 C, the average charge capacity is 364, 334, 313, and 270 mAh g⁻¹, respectively. However, for the LVO, it only shows an average charge capacity of 113, 84, 46, 33, and 23 mAh g⁻¹ as the current densities increase from 0.5 C to 1 C, 5 C, 10 C, and 20 C, respectively. Even at a much higher current density of 50 C, corresponding to a duration of about 40 seconds to finish a discharge/charge cycle, the LVO/C/CNTs can also exhibit the

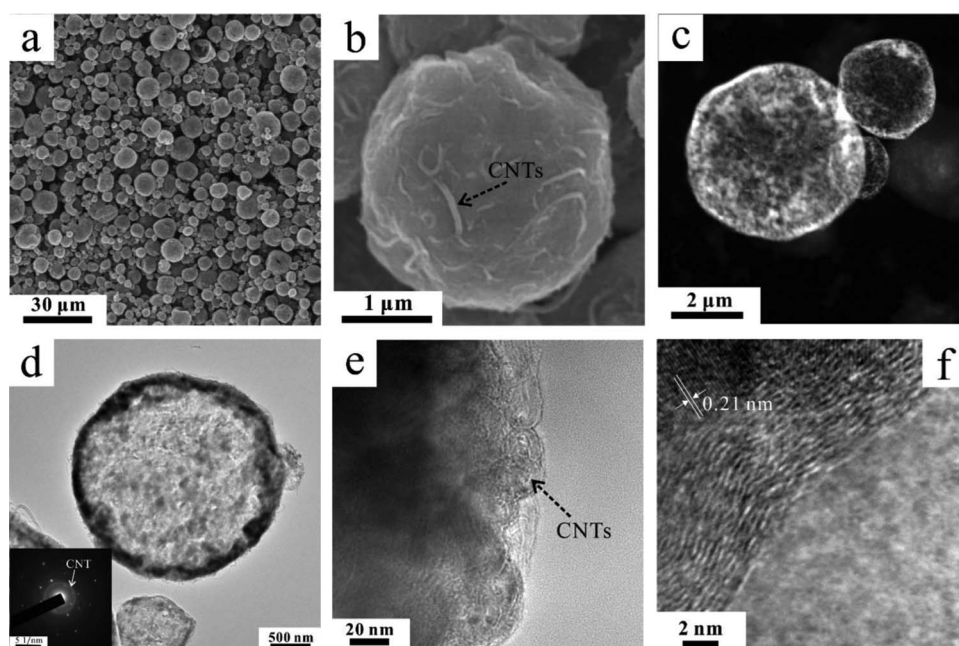


Figure 4. (a, b) SEM images, (c) high-angle annular dark field (HAADF) image, (d, e) TEM images of LVO/C/CNTs. Inset in part c is the SAED pattern of the LVO/C/CNTs particle. (f) HRTEM image of LVO/C/CNTs.

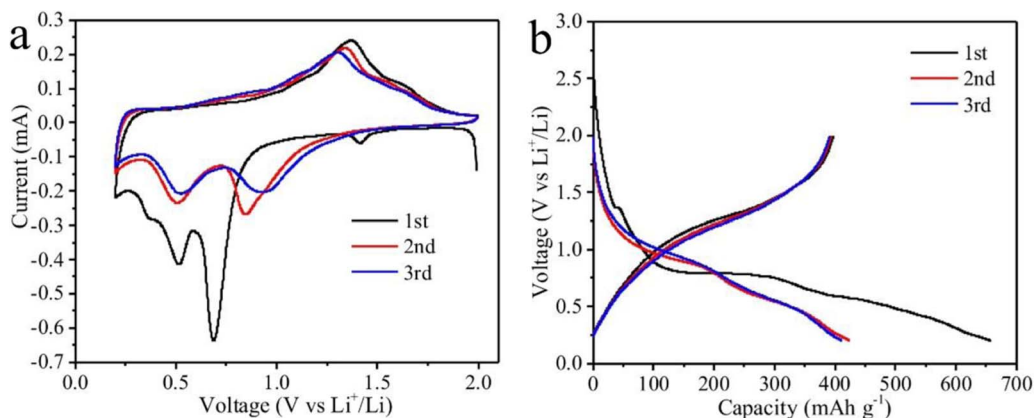


Figure 5. (a) Cyclic voltammograms of LVO/C/CNTs in the first 3 cycles at the sweep rate of 0.2 mV s^{-1} between 0.2 to 2.0 V; (b) Charge-discharge voltage profiles of LVO/C/CNTs in the first 3 cycles at 0.5 C ($1\text{C} = 0.4 \text{ A g}^{-1}$) between 0.2 to 2.0 V.

reversible capacity of 109 mAh g^{-1} , while the capacity of LVO is almost zero. Besides, when the current density returns to 0.5 C, the capacity of LVO/C/CNTs recovers to 378 mAh g^{-1} and maintained at 373 mAh g^{-1} after another 50 cycles, indicating the high cycling stability of LVO/C/CNTs. Cycle performance of the LVO/C/CNTs electrode obtained at 0.5 C with the cutoff voltage window of 0.01–2 V is also investigated (Figure S1). The volumetric specific capacity is also a very important factor for anode materials. As shown in Table S1 and S2, the average volumetric specific capacity of the LVO/C/CNTs electrode is calculated to be $260.1 \text{ mAh cm}^{-3}$, which is close to that of the graphite electrode ($275.1 \text{ mAh cm}^{-3}$).

To further study the cyclability of LVO/C/CNTs, a long-term galvanostatic cycling at 10 C was carried out. As shown in Figures 6b and 6c, encouragingly, a high reversible capacity of 272 mAh

g^{-1} can be maintained after 500 cycles at 10 C (86.1% retention of the 2nd charge capacity). In addition, the coulombic efficiency remains higher than 99% since the 5th cycle. The excellent cycle performance of LVO/C/CNTs has a strong correlation with the specific structure which has enhanced the electronic conductivity and Li^+ ions transmission. Electrochemical performance at high temperature is another critical factor to anode materials for practical application. The LVO/C/CNTs electrode is cycled under the current density of 10 C at the temperature of 45°C . As shown in Figure 6d and S2, after 500 cycles the LVO/C/CNTs electrode retains a reversible capacity of 299 mAh g^{-1} , corresponding to 83.5% retention of the 2nd charge capacity.

Figures 7a and 7b show the cyclic voltammograms of LVO and LVO/C/CNTs at different scan rates from 0.2 to 1 mV s^{-1} . With

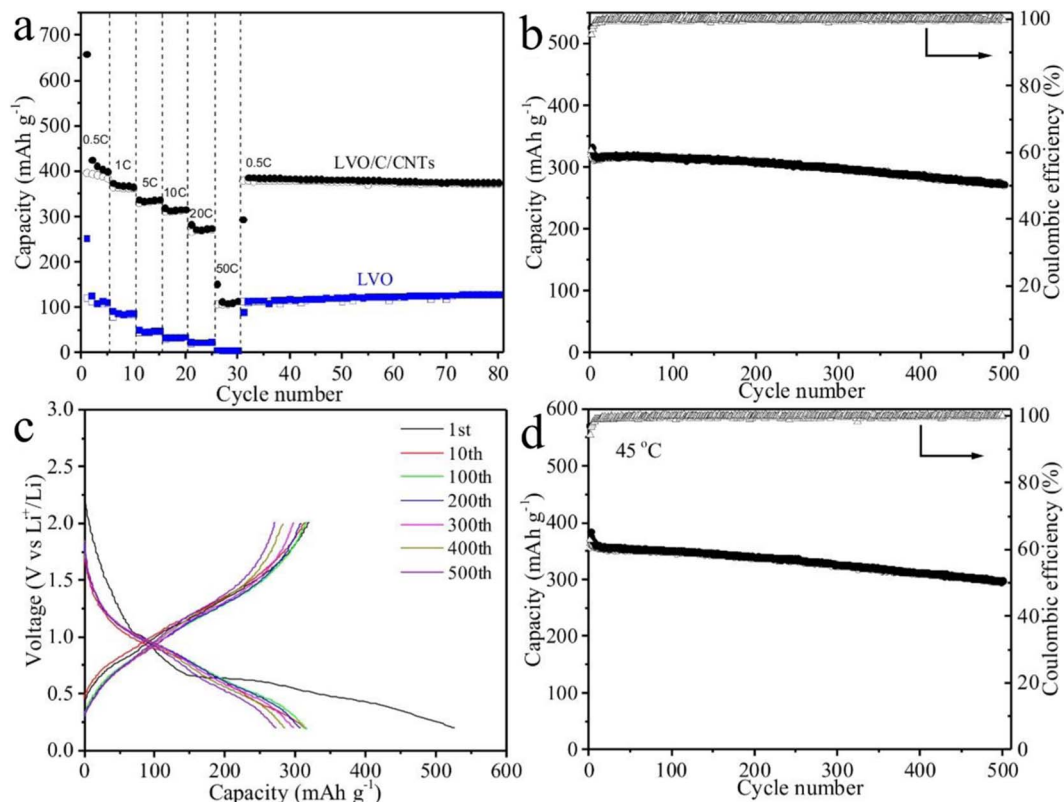


Figure 6. (a) Rate performance of LVO/C/CNTs and LVO at various current densities from 0.5 C to 50 C; (b) Long life capacity retention and (c) typical discharge/charge profiles of LVO/C/CNTs at 10 C for 500 cycles; (d) Cycle performance and coulombic efficiency of LVO/C/CNTs at 45°C and 10 C.

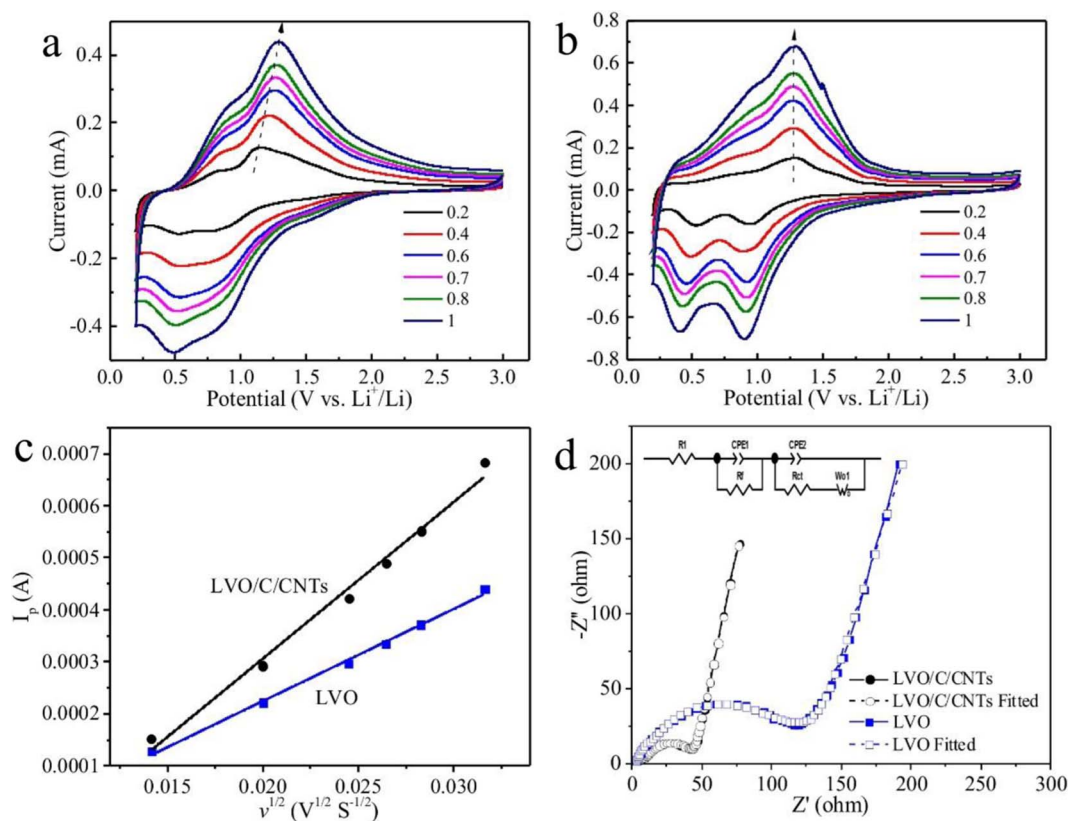


Figure 7. Cyclic voltammery curves of (a) LVO, and (b) LVO/C/CNTs measured at different scan rates ranging from 0.2~1 mV s⁻¹; (c) The plots of peak currents (I_p) as a function of the square root of the scan rates ($v^{1/2}$) for LVO and LVO/C/CNTs; (d) Electrochemical impedance spectroscopy (EIS) of the LVO and LVO/C/CNTs electrodes, the inset shows the equivalent circuit used to fit the plots.

increasing of the scan rate, the anodic peak potential shifts to the higher potential and the cathodic peak potential shifts to the lower potential, respectively. But, the peak potential of LVO/C/CNTs is much less shifted than that of LVO (marked by the arrows), indicating that the polarization of LVO/C/CNTs electrode is less than LVO electrode.³⁰ As shown in Figure 7c, for both samples, the peak current (I_p) exhibits a beautiful linear relation with the square root of the scan rate ($v^{1/2}$), indicating the intercalation process of lithium ions into Li_3VO_4 is diffusion-controlled.³¹ Thus the Li^+ ions diffusion is a key factor to the electrode kinetics.³² The apparent diffusion coefficient of Li^+ ions (D) can be obtained by the Randles-Sevcik equation:^{12,33,34}

$$I_p = 0.4463n^{3/2}F^{3/2}R^{-1/2}T^{-1/2}AD^{1/2}C^0v^{1/2} \quad [2]$$

Where I_p is the peak current for the anodic process, n is the charge transfer number, F is Faraday constant, R is the gas constant, T is the absolute temperature, A is the effective surface area of the electrode, C^0 is Li^+ ions concentration in the cathode, and v is the scan rate. By inserting the slope of fitting line (Figure 7c) into Equation 2, the apparent Li^+ ions diffusion coefficient of LVO/C/CNTs was calculated to be $1.27 \times 10^{-11} \text{ cm}^2 \text{ s}^{-1}$, which is much higher than that of LVO ($4.41 \times 10^{-12} \text{ cm}^2 \text{ s}^{-1}$). The higher apparent Li^+ ions diffusion coefficient should be attributed to the hollow and porous morphology of the LVO/C/CNTs particles, which is favorable for Li^+ ions diffusion.^{18,26,35}

Electrochemical impedance spectroscopy (EIS) measurements were carried out to further investigate the charge-transport kinetics for both samples. As shown in Figure 7d, each Nyquist plot consists of a dispersed semicircle and an inclined line. The intercept in high-frequency can be attributed to the electrolyte resistance (R_1).¹³ The dispersed semicircle includes two compressed semicircles: the resistance of SEI film (R_f) in the high-frequency range, and the charge-transfer resistance (R_{ct}) in the high to medium-frequency

region, respectively.^{36,37} The inclined line in the low-frequency range can be considered as the Warburg impedance.³⁸ The Nyquist plots are fitted by using the equivalent circuit model (inset in Figure 7d). More detailed simulated kinetic parameters are shown in Table I. Clearly, the R_{ct} of LVO/C/CNTs is much smaller than that of LVO, indicating a faster charge-transfer process. The higher apparent Li^+ ions diffusion coefficient and smaller charge-transfer resistance of LVO/C/CNTs are favorable for rapid charge and discharge.

Full-cells combining the commercial $\text{LiNi}_{0.5}\text{Co}_{0.2}\text{Mn}_{0.3}\text{O}_2$ cathode with our LVO/C/CNTs anode have been assembled. The full cell with capacity limited by LVO/C/CNTs were galvanostatically cycled between 1.5 and 4.3 V at 1 C (0.4 A g^{-1}). As shown in Figure 8, the LVO/C/CNTs- $\text{LiNi}_{0.5}\text{Co}_{0.2}\text{Mn}_{0.3}\text{O}_2$ full cell give an operating voltage of around 3.0 V and can deliver a reversible discharge capacity of 395 mAh g⁻¹ after 50 cycles at 1C.

The outstanding rate capability and cyclability of LVO/C/CNTs can be elucidated as follows: (1) The hollow and porous structure of LVO/C/CNTs can shorten diffusion paths of Li^+ ions and enhance the penetration of electrolyte, leading to faster Li^+ ions diffusion; (2) The hollow structure can provide extra free space to better relax the structure stress during Li^+ insertion, leading to better structural stability; (3) Carbon-coated Li_3VO_4 nanocrystals are interconnected by CNTs to form an integrated electronic conducting particle, leading to faster electrons transfer. Because of these synergistic effects, LVO/C/CNTs

Table I. Equivalent-circuit parameters and errors obtained from fitting the experimental impedance spectra.

Sample	R_1 (Ω)	Error (%)	R_f (Ω)	Error (%)	R_{ct} (Ω)	Error (%)
LVO	2.95	1.41	11.44	1.12	85.79	0.69
LVO/C/CNTs	2.62	1.13	7.94	0.44	29.34	0.81

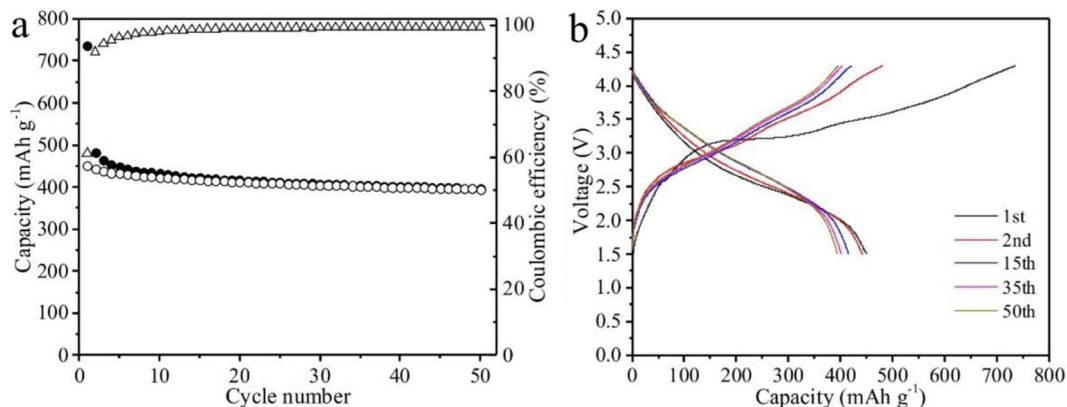


Figure 8. (a) Cycle performance and (b) typical discharge/charge profiles of the LVO/C/CNTs-LiNi_{0.5}Co_{0.2}Mn_{0.3}O₂ full cell.

exhibits much improved electrochemical performance than pristine LVO.

Conclusions

In summary, LVO/C/CNTs composites with hollow structure have been successfully synthesized by a one-pot, spray drying method. The LVO/C/CNTs composites show a much higher apparent Li⁺ ions diffusion coefficient ($1.27 \times 10^{-11} \text{ cm}^2 \text{ s}^{-1}$), than the pristine LVO ($4.41 \times 10^{-12} \text{ cm}^2 \text{ s}^{-1}$). Meanwhile, the charge-transfer resistance of LVO/C/CNTs (29.34 Ω) is much smaller than the pristine LVO (85.79 Ω). The faster kinetics process offers LVO/C/CNTs much improved electrochemical performance. As a result, LVO/C/CNTs composites exhibit superior rate capability with 109 mAh g^{-1} at 50 C. After 500 cycles at 10 C, the reversible capacity of 272 mAh g^{-1} can be maintained (86.1% retention of the 2nd charge capacity). Moreover, the synthetic method is facile and scalable, thus LVO/C/CNTs composites can be a promising anode material for large-sized LIBs.

Acknowledgments

The authors gratefully acknowledge financial support from National Natural Science Foundation of China (21273185 and 21321062) and Key Project of Science and Technology of Xiamen (3502ZZ20141008). The authors also wish to express their thanks to Prof. Daiwei Liao of Xiamen University for his valuable discussion and suggestion.

References

- J. M. Tarascon and M. Armand, *Nature*, **414**, 359 (2001).
- Y. Yang, J. Li, D. Chen, T. Fu, D. Sun, and J. Zhao, *ChemElectroChem*, **3**, 757 (2016).
- A. Birozzi, M. Copley, J. von Zamory, M. Pasqualini, S. Calcaterra, F. Nobili, A. D. Cicco, H. Rajantie, M. Briceno, E. Bilb , L. Cabo-Fernandez, L. J. Hardwick, D. Bresser, and S. Passerini, *J. Electrochem. Soc.*, **162**, A2331 (2015).
- M. He, E. Castel, A. Laumann, G. Nussli, P. Nov k, and E. J. Berg, *J. Electrochem. Soc.*, **162**, A870 (2015).
- G. N. Zhu, H. J. Liu, J. H. Zhuang, C. X. Wang, Y. G. Wang, and Y. Y. Xia, *Energy Environ. Sci.*, **4**, 4016 (2011).
- Y. B. Shen, M. Sondergaard, M. Christensen, S. Birgisson, and B. B. Iversen, *Chem. Mater.*, **26**, 3679 (2014).
- G. N. Zhu, L. Chen, Y. G. Wang, C. X. Wang, R. C. Che, and Y. Y. Xia, *Adv. Funct. Mater.*, **23**, 640 (2013).
- H. Li, X. Liu, T. Zhai, D. Li, and H. Zhou, *Adv. Energy Mater.*, **3**, 428 (2013).
- W.-T. Kim, Y. U. Jeong, Y. J. Lee, Y. J. Kim, and J. H. Song, *J. Power Sources*, **244**, 557 (2013).
- Z. Liang, Z. Lin, Y. Zhao, Y. Dong, Q. Kuang, X. Lin, X. Liu, and D. Yan, *J. Power Sources*, **274**, 345 (2015).
- J. Liu, P.-J. Lu, S. Liang, J. Liu, W. Wang, M. Lei, S. Tang, and Q. Yang, *Nano Energy*, **12**, 709 (2015).
- C. K. Zhang, H. Q. Song, C. F. Liu, Y. G. Liu, C. P. Zhang, X. H. Nan, and G. Z. Cao, *Adv. Funct. Mater.*, **25**, 3497 (2015).
- J. Zhang, S. Ni, J. Ma, X. Yang, and L. Zhang, *J. Power Sources*, **301**, 41 (2016).
- Z. Jian, M. Zheng, Y. Liang, X. Zhang, S. Gheyhani, Y. Lan, Y. Shi, and Y. Yao, *Chem. Commun.*, **51**, 229 (2015).
- Y. Shi, J.-Z. Wang, S.-L. Chou, D. Wexler, H.-J. Li, K. Ozawa, H.-K. Liu, and Y.-P. Wu, *Nano Lett.*, **13**, 4715 (2013).
- S. Hu, Y. F. Song, S. Y. Yuan, H. M. Liu, Q. J. Xu, Y. G. Wang, C. X. Wang, and Y. Y. Xia, *J. Power Sources*, **303**, 333 (2016).
- Q. Li, J. Sheng, Q. Wei, Q. An, X. Wei, P. Zhang, and L. Mai, *Nanoscale*, **6**, 11072 (2014).
- Z. Y. Wang, L. Zhou, and X. W. Lou, *Adv. Mater.*, **24**, 1903 (2012).
- K. Okuyama, M. Abdullah, I. W. Lenggoro, and F. Iskandar, *Adv. Powder Technol.*, **17**, 587 (2006).
- N. Tsapis, D. Bennett, B. Jackson, D. A. Weitz, and D. A. Edwards, *PNAS*, **99**, 12001 (2002).
- P. Tartaj, J. M. Amarilla, and M. B. Vazquez-Santos, *Chem. Mater.*, **28**, 986 (2016).
- D. Zhao and M. Cao, *ACS Appl. Mater. Interfaces*, **7**, 25084 (2015).
- Y. Chen, X. Li, K. Park, J. Song, J. Hong, L. Zhou, Y.-W. Mai, H. Huang, and J. B. Goodenough, *J. Am. Chem. Soc.*, **135**, 16280 (2013).
- L. L. Zhang, X. Zhao, M. D. Stoller, Y. Zhu, H. Ji, S. Murali, Y. Wu, S. Perales, B. Clevenger, and R. S. Ruoff, *Nano Lett.*, **12**, 1806 (2012).
- L. Shen, C. Yuan, H. Luo, X. Zhang, K. Xu, and Y. Xia, *J. Mater. Chem.*, **20**, 6998 (2010).
- L. J. Xi, H.-E. Wang, Z. G. Lu, S. L. Yang, R. G. Ma, J. Q. Deng, and C. Y. Chung, *J. Power Sources*, **198**, 251 (2012).
- S. Ni, J. Zhang, J. Ma, X. Yang, and L. Zhang, *J. Power Sources*, **296**, 377 (2015).
- S. Ni, X. Lv, J. Ma, X. Yang, and L. Zhang, *Electrochim. Acta*, **130**, 800 (2014).
- J. B. Chang, X. K. Huang, G. H. Zhou, S. M. Cui, P. B. Hallac, J. W. Jiang, P. T. Hurley, and J. H. Chen, *Adv. Mater.*, **26**, 758 (2014).
- Y. C. Yang, B. H. Qiao, X. M. Yang, L. B. Fang, C. C. Pan, W. X. Song, H. S. Hou, and X. B. Ji, *Adv. Funct. Mater.*, **24**, 4349 (2014).
- J. Q. Deng, J. Pan, Q. R. Yao, Z. M. Wang, H. Y. Zhou, and G. H. Rao, *J. Power Sources*, **278**, 370 (2015).
- Y. Y. Mi, P. Gao, W. Liu, W. D. Zhang, and H. H. Zhou, *J. Power Sources*, **267**, 459 (2014).
- C.-K. Back, R.-Z. Yin, and Y.-S. Kim, *J. Electrochem. Soc.*, **160**, A1551 (2013).
- J. Lu, X. Fan, C. Zhou, Z. Liu, F. Zheng, K. S. Lee, and L. Lu, *J. Electrochem. Soc.*, **163**, A197 (2016).
- C. Lin, M. O. Lai, H. Zhou, and L. Lu, *Phys. Chem. Chem. Phys.*, **16**, 24874 (2014).
- L. Cheng, X.-L. Li, H.-J. Liu, H.-M. Xiong, P.-W. Zhang, and Y.-Y. Xia, *J. Electrochem. Soc.*, **154**, A692 (2007).
- G.-N. Zhu, C.-X. Wang, and Y.-Y. Xia, *J. Electrochem. Soc.*, **158**, A102 (2011).
- Y. Yang, D. Chen, B. Liu, and J. Zhao, *ACS Appl. Mater. Interfaces*, **7**, 7497 (2015).